

Physics-dynamics coupling with element-based high-order Galerkin methods: quasi equal-area physics grid

ADAM R. HERRINGTON*

School of Marine and Atmospheric Sciences, Stony Brook University, State University of New York, Stony Brook, New York.

PETER H. LAURITZEN

Climate and Global Dynamics, National Center for Atmospheric Research, 1850 Table Mesa Drive, Boulder, Colorado, USA.

MARK A. TAYLOR

Sandia National Laboratories, Albuquerque, New Mexico, USA.

PAUL A. ULLRICH

Department of Land, Air and Water Resources, University of California, Davis, California, USA

JULIO T. BACMEISTER

Climate and Global Dynamics, National Center for Atmospheric Research, 1850 Table Mesa Drive, Boulder, Colorado, USA.

STEVE GOLDHABER

Climate and Global Dynamics, National Center for Atmospheric Research, 1850 Table Mesa Drive, Boulder, Colorado, USA.

KEVIN A. REED

School of Marine and Atmospheric Sciences, Stony Brook University, State University of New York, Stony Brook, New York.

ABSTRACT

Enter the text of your abstract here.

1. Introduction

An increasing number of numerical methods publications in the atmospheric science literature concern transport, shallow-water, and three-dimensional models employing element-based high-order Galerkin discretizations such as finite-element and discontinuous Galerkin methods (for an introduction to these methods see, e.g., Durran 2010; Nair et al. 2011). Some global models based on Galerkin methods have reached a level of maturity for which they are being considered for next

generation climate and weather models due to their inherent conservation properties, high-order accuracy (for smooth problems), high parallel efficiency, high processor efficiency, and geometric flexibility facilitating mesh-refinement applications. NCAR's Community Atmosphere Model (CAM; Neale et al. 2010) offers a dynamical core based on continuous Galerkin finite elements (Taylor and Fournier 2010), referred to as CAM-SE (CAM Spectral Elements; Dennis et al. 2012; Taylor et al. 2008; Lauritzen et al. 2017). CAM-SE is, in particular, being used for high resolution climate modeling (e.g., Small et al. 2014; Bacmeister et al. 2013; Reed et al. 2015) and static mesh-refinement applications (e.g., Fournier et al. 2004; Zarzycki et al. 2014a,b; Guba et al. 2014; Rhoades et al. 2016). Other examples of models based on high-

*Corresponding author address: Peter H. Lauritzen, Climate and Global Dynamics, National Center for Atmospheric Research, 1850 Table Mesa Drive, Boulder, Colorado, USA.
E-mail: pel@ucar.edu

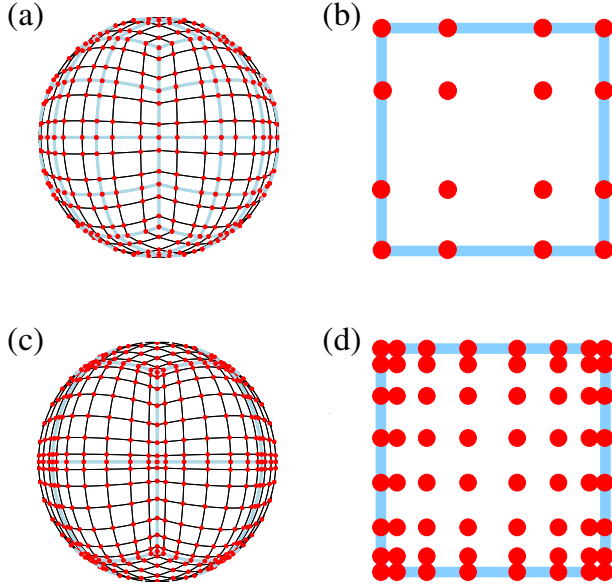


FIG. 1. Example of CAM-SE GLL quadrature grids, marked with red filled circles, (a & c) on the cubed-sphere and (b & d) in an element. (a)-(b) and (c)-(d) use 4×4 ($np = 4$) and 8×8 ($np = 8$) GLL quadrature points in each element, respectively. (a) and (c) have the same average grid-spacing at the Equator (7.5°) which is obtained by using (a) 4×4 ($ne = 4$) and (b) 2×2 ($ne = 2$) elements on each cubed-sphere face/panel, respectively. The element boundaries are marked with thick light blue lines. The grid configurations shown on (a) and (c) are referred to as $ne4np4$ and $ne2np8$, respectively.

order Galerkin methods that are being considered for ‘operational’ weather-climate applications are Giraldo and Restelli (2008), Nair et al. (2009) and Brdar et al. (2013).

Traditionally the state of the atmosphere passed to the sub-grid-scale parameterizations (also referred to as *physics*) for models based on finite-volume and finite-difference methods has been the cell-averaged state in each control volume and the grid-point value, respectively. For the regular latitude-longitude, cubed-sphere and icosahedral grids the distance between the grid-points is gradually varying for finite-volume/finite-difference discretizations. If the same physics-dynamics coupling paradigm is applied to high-order element-based Galerkin methods, the state of the atmosphere passed to physics would be evaluated at the quadrature points. In the case of CAM-SE these are the Gauss-Lobatto-Legendre (GLL) quadrature points. Having the physics and dynamics grids coincide is obviously convenient since no interpolation is needed (which could disrupt conservation properties) and the number of degrees of freedom on both grids is exactly the same. A unique aspect of the high-order quadrature rules is that the nodes within an element are not equally spaced. For example, Figure 1 shows GLL points on an individual element of a cubed-sphere grid for degree 3

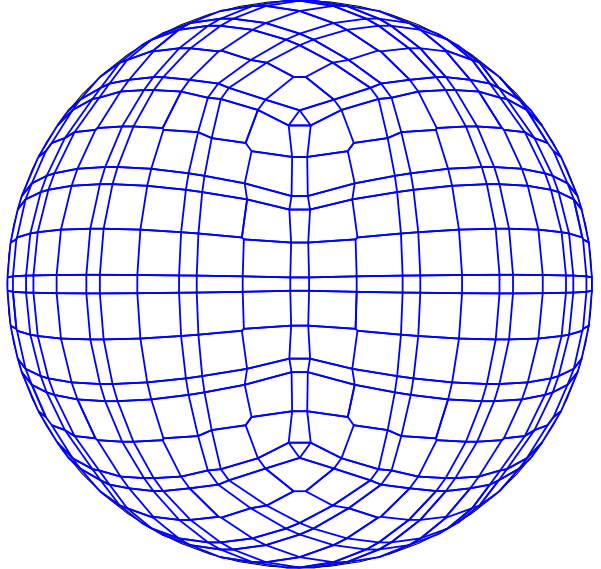


FIG. 2. An example of control volumes constructed around GLL quadrature points (NE4NP4) so that the spherical area of the control volumes exactly match the quadrature weight multiplied by the metric factor.

($np = 4$ quadrature points) and degree 7 ($np = 8$ quadrature points) Lagrange polynomial basis in CAM-SE. Both grids have the same average resolution on the sphere (due to different number of elements), however, the higher the order of the quadrature rule the less equi-distant are the quadrature points. GLL quadrature points cluster near the edges and, in particular, the corners of the elements.

Parameterizations use the state of the atmosphere from the dynamical core as the large-scale state for computing sub-grid-scale processes. For example, the dynamical core defines the large-scale environment for closing quasi-equilibrium-type convection schemes (Arakawa and Schubert 1974). One may think of the dynamical core state as the average state of the atmosphere over a control volume as inherent to finite-volume methods. For finite-difference methods the point value is thought of as representative for the atmospheric state in the vicinity of the point value and one can usually associate a volume with the grid-point. Hence the physics grid (the grid on which the state of the atmosphere is evaluated and passed to physics) and the dynamics grid (the grid the dynamical core uses) coincide. If we apply this concept to GLL quadrature values then a volume associated with the quadrature point should be defined. An example of that is shown on Figure 2 where control volumes have been defined around the quadrature points so that the spherical area of the control volumes exactly match the Gaussian weight multiplied by the metric term (these weights are used for integrating the basis func-

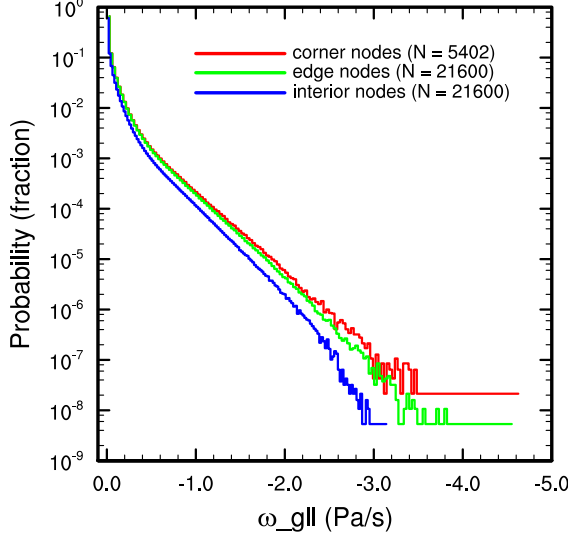


FIG. 3. Probability density distribution of instantaneous upward ω , conditionally sampled based on interior, edge and corner node control volumes. Figure is constructed from one year of six hourly data, $\pm 10^\circ$ from the equator from the equator and at all vertical levels. Note the consistently larger magnitude ω values for boundary nodes, compared to interior nodes. Grid imprinting is exacerbated since the irregular state is commuted through the physical parameterizations.

tions over the elements and can therefore, in this context, be interpreted as areas). [Mark: could we be mathematically more rigorous? perhaps an appendix describing the iterative algorithm?] This grid is used in the NCAR CESM (Community Earth System Model) coupler for passing states between ocean, atmosphere and land components since the current remapping method is finite-volume based and therefore requires control volumes¹. Hence the components ‘see’ an irregular atmospheric grid. Similarly, the parameterizations in the atmosphere ‘see’ a state that is anisotropically sampled in space (see Figure 1 and 5 in Kim et al. 2008). Physical inconsistencies may arise, for example, if assumptions inherent to sub-grid parameterizations break down only at the smallest control volumes of the grid.

It would be incorrect to interpret the irregular size of control volumes in Figure 2 as an equivalent spread in the scales of motion resolved by the dynamical core. The scales of motion are defined by the degree of the Lagrange basis in each element, and the nodes may be viewed as irregularly spaced samples of an underlying spectrally truncated state. From this perspective, one would expect the solution to be independent of control volume size. An aqua-planet simulation (Neale and Hoskins 2000; Medeiros et al. 2016) is carried out using CAM-SE (Figure 3), and the probability density distribution of the up-

ward vertical pressure velocity (ω), conditionally sampled based on three categories - ‘interior nodes’, with their large grid cell areas, and ‘edge’ and ‘corner’ nodes with their characteristically smaller grid cell areas - is shown in Figure 3. There is an apparent dependence on control volume size, with interior nodes being characteristically sluggish and initially at odds with our expectation. However, the lack of a distinction between ‘corner’ and ‘edge’ solutions is inconsistent with our expectation. It turns out, that ‘corner’ and ‘edge’ solutions are similar because they have something else in common - they both lie on an element boundary. The division of solutions shown in Figure 3 is actually between whether a node is, or is not situated on an element boundary, and is a nuanced signature of element-based Galerkin methods.

The quadrature grid in high-order element-based Galerkin methods is defined to perform mathematical operations on the basis functions, e.g., computing gradients and integrals, rather than evaluating the state variables for physics-dynamics coupling. While the interior quadrature nodes are high-order C^∞ , the smoothness of boundary nodes are constrained by the need to patch neighboring solutions together to form a global solution. This boundary exchange results in a C^0 degradation at element boundaries (Figure 4). Through evaluating the physics at the nodal points, strong grid-scale forcing or oscillatory behavior near an element boundary may exacerbate the discontinuity (Figure 4). The greater magnitude vertical motion of boundary nodes in Figure 3 is therefore due to the systematically tighter pressure gradients on element boundaries. One may argue that it would be more consistent to integrate the basis functions over quasi-equal area control volumes within each element and pass those control volume average values to physics rather than irregularly spaced quadrature point values. In this case when integrating basis functions over control volumes a grid-cell average value is more representative of the values near the extrema at the element boundary than the quadrature point value. The relationship between the nodal values, the basis functions and the proposed control volumes is illustrated schematically in one-dimension in Figure 5).

It is the purpose of this paper to document the design of CAM-SE with an approximately isotropic physics grid (CAM-SE-PG) in which we separate physics and dynamics grids as illustrated in one dimension above. The mapping procedures used in CAM-SE-PG are presented in Section 2. Idealized model configurations with and without topography are presented in Section 3, illustrating the marked reduction in grid imprinting in CAM-SE-PG compared with the default CAM-SE. Section 4 contains a discussion of results and concluding remarks.

¹it is noted that methods exist that do not require control volumes for conservative interpolation (Ullrich and Taylor 2015)

2. Methods

Here we focus on CAM-SE, however, in principle the methods apply to any element-based high-order Galerkin model. The physics grid in CAM-SE is defined by subdividing each element using equi-angular gnomonic coordinate lines to define the sides of the physics grid control volumes. Note that the element boundaries are defined by equi-angular gnomonic grid lines. The notation $pg = 3$ refers to the configuration where the elements are divided into $pg \times pg = 3 \times 3$ quasi equal-area physics grid cells (see Figure 8). Defining the physics grid by sub-diving elements makes it possible to use the same infrastructure as used for the quadrature point values thereby facilitating its implementation in CAM-SE. Here we make use of the $ne30np4$ and $ne30pg3$ grids that use GLL quadrature point physics grid (physics and dynamics grid coincide), and the same ($pg = 3$) resolution quasi equal-area physics grids, respectively. In all configurations we use degree 3 Lagrange basis ($np = 4$) and $ne \times ne = 30 \times 30$ elements on each cubed-sphere panel resulting in an average GLL quadrature point spacing at the Equator of 1° . Vertical grid spacing is the standard CAM5 configuration ($nlev = 30$).

A consequence of separating physics and dynamics grids is that the atmospheric state must be mapped to the physics grid and the physics tendencies must be mapped back to the dynamics grid. Note that tendencies and not an updated state is mapped back to the dynamics grid. If one were to map an updated state the errors in the mapping process may adversely affect the simulation, e.g., in the case of no physics forcing there will be a non-zero ‘physics forcing’ entirely due to the errors in the mapping algorithm.

In a climate model setting it is important that this process does not violate important conservation properties such as:

- mass-conservation,
- shape-preserving (monotone), i.e. the mapping method does not introduce new extrema in the interpolated field, in particular, negatives,
- consistency, i.e. the mapping preserves a constant.

Other properties that may be important, but not pursued here, is energy conservation and axial angular momentum conservation. It may be desirable to preserve the high-order of the basis functions during the mapping process so that the mapping is high-order accurate for smooth fields and less information is lost during the mapping process.

• description of PHIS

a. Remapping state: GLL grid \rightarrow physics grid

The state variables that need to be mapped from the GLL grid to the physics grid are temperature $T^{(GLL)}$

and velocity components $(u^{(GLL)}, v^{(GLL)})$. Temperature is mapped by integrating the SE basis function representation of $T^{(GLL)} \times \Delta p^{(GLL)}$ and $\Delta p^{(GLL)}$ over the physics grid control volumes. The temperature on the physics grid is recovered from $\frac{T^{(phys)} \times \Delta p^{(phys)}}{\Delta p^{(phys)}}$. This mapping method conserves dry thermal energy $c_p^{(d)} T^{(GLL)} \times \Delta p^{(GLL)}$, where $c_p^{(d)}$ is the heat capacity for dry air at constant pressure, in each element. The velocity vectors are transformed from spherical coordinates to contravariant components (see, e.g., section 3.2 in Lauritzen et al. 2017) and the basis function representation of each contravariant velocity component is evaluated at the centerpoint of the physics grid control volumes. Thereafter the vectors are transformed back to spherical coordinates. Since the atmospheric state mapped from dynamics to physics grid is based on the high-order SE basis functions, the loss of accuracy in transferring the state from GLL to physics grid is minimized.

b. Remapping: physics grid \rightarrow GLL grid

The CAM physics package returns tendencies for temperature $f_T^{(phys)}$, velocity components $(f_u, f_v)^{(phys)}$, water vapor $f_Q^{(phys)}$, other tracers $f_q^{(phys)}$, and surface pressure $f_{PS}^{(phys)}$. The latter forcing is due to the vertical coordinate in CAM-SE being based on ‘wet’ pressure (dry air mass plus the weight of water vapor) so if there is a change in moisture in the column then the ‘wet’ surface pressure PS changes whereas the dry air mass (surface pressure) remains constant (see section 3.1.8 ‘Adjustment of pressure to include change in mass of water vapor’ in Neale et al. 2010).

As for the dynamics to physics grid mapping, conservation is important and we therefore mass-weight the variables being mapped. For that Δp on the physics and dynamics grid is needed. Mapping the updated surface pressure on the physics grid to the dynamics grid is not desirable: first of all, if there is no tendency on surface pressure then the mapped surface pressure on the GLL grid will be different from the surface pressure on the GLL grid before calling physics. As mentioned before, this is equivalent to having a spurious forcing on PS entirely due to errors in the mapping algorithm. Secondly, conservation properties will result unless the GLL grid surface pressure is overwritten by the mapped PS from the physics grid to the dynamics grid. To ensure conservation and spurious forcing due to mapping errors the following algorithm is adopted for the mass-weighting.

Let Δp_{phys} be the updated pressure level thickness returned by physics. Map water-vapor mass $\Delta p_{phys} f_Q^{(phys)}$ from the physics to the dynamics grid using a conservative, consistent, and shape-preserving method (see below) resulting in $\Delta p_{phys} f_Q^{(phys)}$. This variable is the sur-

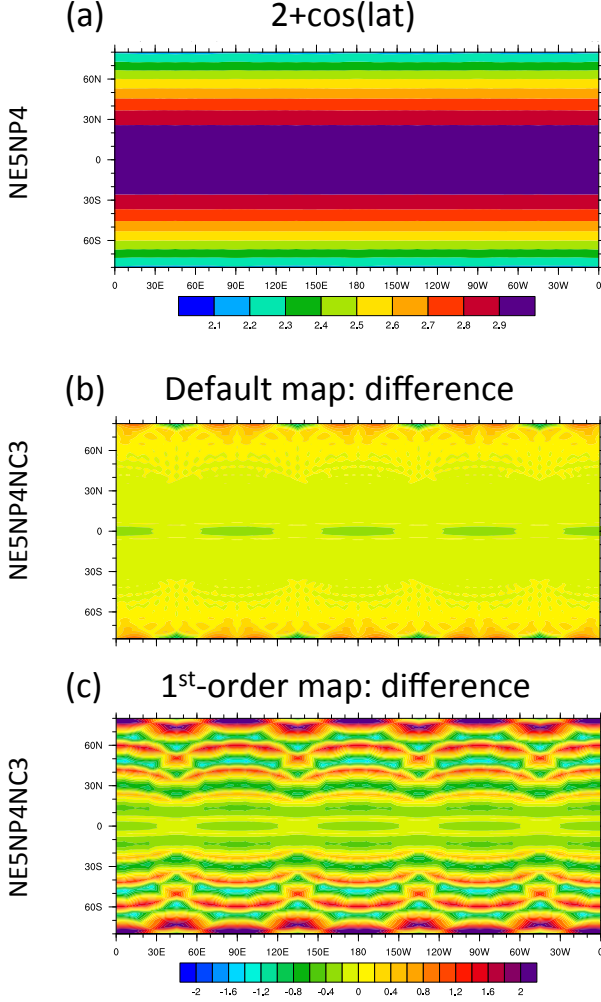


FIG. 6. (a) Smooth function ($2 + \cos(\theta)$) initialized on the *NE5NP4* GLL grid. (b) and (c) show the difference between the interpolated field and the analytical value at the physics grid cell center. The interpolation is from the *NE5NP4* GLL grid to the *NE5NP4NC3* physics grid (both have an approximate grid spacing of 6°). In (b) the interpolation algorithm is the default algorithm that is higher-order for smooth fields, shape-preserving, consistent, and mass-conservative. (c) is the same as (b) but using the first-order mapping method. All data has been bilinearly interpolated to a 1° regular latitude-longitude grid for plotting.

face pressure tendency on the GLL grid, $f_{PS}^{(GLL)}$. Now take the surface pressure on the GLL grid before calling physics $p_s^{(GLL)}$ and add the surface pressure tendency $\Delta t PS^{(GLL)}$. This updated surface pressure $p_s^{(GLL)}$ defines the updated pressure-level thicknesses $\Delta p^{(GLL)}$. We use the physics updated pressure level thickness on the physics grid $\Delta p^{(phys)}$ for the mass-weighting of the physics tendencies $f_i^{(phys)}$, where $i = T, Q, q, u_x, u_y, u_z$, and $\Delta p^{(GLL)}$ for recovering the tendencies after mapping. The velocity

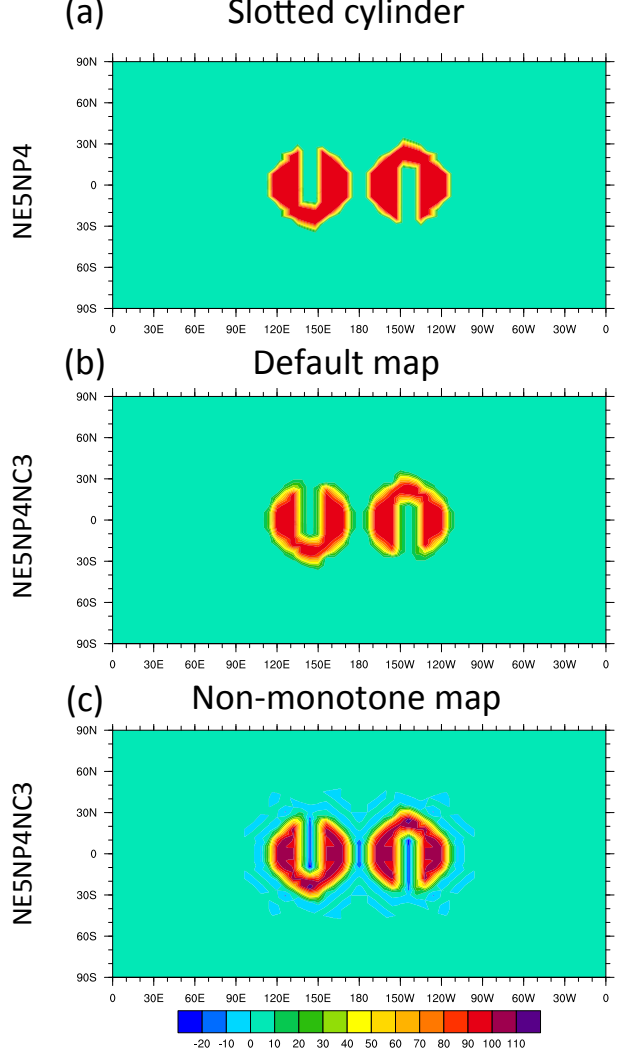


FIG. 7. (a) Slotted-cylinder distribution initialized on the *NE5NP4* GLL grid (approximately 6° resolution). (b) Default mapping of the *NE5NP4* GLL grid data to the physics grid *NE5NP4NC3*. (c) Same as (b) but using the non-monotone map. All data has been bilinearly interpolated to a 1° regular latitude-longitude grid for plotting.

forcing is transformed into a Cartesian coordinate system vector as for the dynamics to physics grid mapping.

1) MAPPING ALGORITHM

[Paul: we are just using low-order map? would it be easy to switch to higher-order?] To build the non-monotone “first guess” map from the finite volume physics grid to the finite element dynamics grid, a continuous polynomial reconstruction of degree $n_c - 1$ (and order n_c) is built that exactly interpolates the volume averaged values in each physics grid element. For the monotone “first

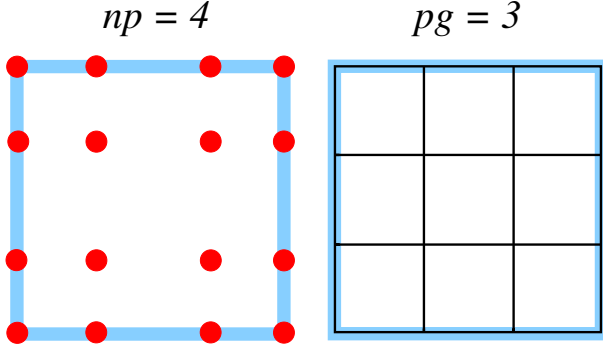


FIG. 8. A graphical illustration of the relationship between Gauss-Lobatto-Legendre quadrature grid for $np = 4$ (left) and ‘equal-area’ finite-volume grid with $pg = 3$.

guess” map, a second-order bilinear reconstruction is instead employed that interpolates the density field at the center of each finite volume. In each case the reconstruction is then sampled at each of the Gauss-Lobatto-Legendre nodes of the dynamics grid.

3. Results

4. Results

The CAM aqua-planet reference configuration (Neale and Hoskins 2000; Medeiros et al. 2016) consists of an ocean covered planet in a perpetual equinox, with fixed, zonally symmetric SST temperatures idealized after the present day climatology. Two year long aqua-planet simulations are performed, using CAM-SE in the *ne30np4* default configuration, and with the *ne30pg3* physics grid configuration. A plot similar to Figure 3 is constructed for the *ne30pg3* simulation, in which a probability density distribution of upward *omega* in the deep tropics is conditionally sampled based on location within the element. In the *ne30pg3* configuration, the sampling is based on a grid cell index 1-9, corresponding to the control volume location within the element (Figure 9). Through the use of the physics grid, the dynamical state appears independent of location within the element, a marked improvement over the *ne30np4* (Figure 3). Since the state is independent of in-element location, it follows that the physics forcing, which is evaluated from the state, should also be independent of within-element location. The low-level, mean and variance of the physics tendencies in the two aqua-planet simulations are shown in Figure 10. The mean physics tendencies contains modest grid imprinting in the default configuration, while in the variance field, grid imprinting is both ubiquitous and unmistakable (Figure 10). The variance is larger on boundary nodes (Figure 10), resulting in a clear ‘stitching’ pattern resembling the cube-sphere grid. In *ne30pg3*, the grid imprinting is all but eliminated based

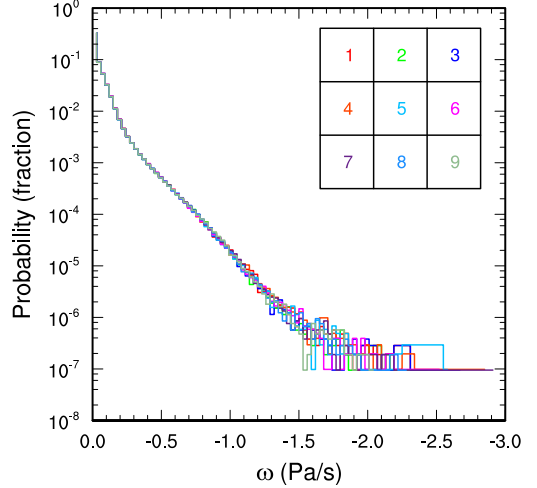
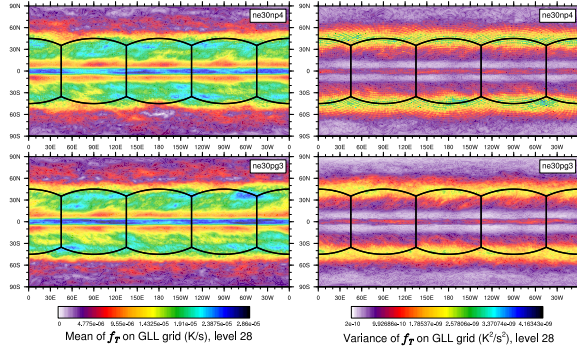


FIG. 9. Similar to Figure 3, but the state is conditionally sampled according to *ne30pg3* control volume location within each element (1-9). Probability density distribution computed from one year of 6-hourly data $\pm 10^\circ$ from the equator, and at all vertical levels. Through the use of the *ne30pg3* physics grid, the state is now independent of in-element location.

on the mean and variance of the physics tendencies (Figure 10).

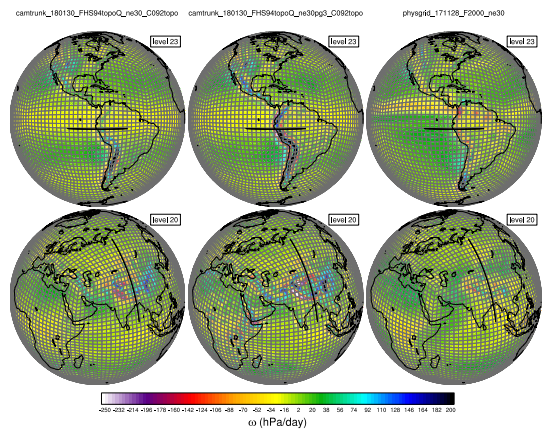
Grid imprinting associated with the flow around obstacles is more problematic than that encountered on the aqua-planets. In order to diagnose grid imprinting associated with topographic flow, an idealized held-suarez configuration (Held and Suarez 1994) is outfitted with real world topography, and ran for a year using the *ne30np4* and *ne30pg3* configurations. Figure 11 shows the mean *omega* at two different vertical levels in the middle troposphere. At higher latitudes (such as southern Andes), the flow is smooth, conforming reasonably to the underlying topography. At lower latitudes, over the Andes or the Himalayas, there is a clear preference for larger magnitude vertical motion to occur at the element boundaries. The vertical structure of *omega* in regions of strong grid-imprinting is depicted in Figure 12, which are great-circle distance-pressure transects over the Andes and Himalayas. The *omega* field indicates large magnitude upward motion occurs as the flow approaches the foot of a topographic obstacle. Compensating downward motion tends to occur



cur about 2 GLL nodes downwind of the strong upward motion (although sometimes they form upwind). The full troposphere upward-downwawrd couplets are an indication that grid imprinting due to topography is enhanced in regions of weak stratification, such as occurs in the deep tropics, with forced upslope flow facilitating the release of gravitational instability. The greater magnitude vertical motion is a result of the characteristically tighter pressure gradients at element boundaries.

The grid-imprinting tends to be exaggerated in the modified held-suarez configuration, compared to more realistic configurations using a complete physical parameterization package. Figure 11 depicts the ω field in an AMIP simulation, which contains less grid imprinting compared to the Held-Suarez configuration through the use of the CAM6 physics pacakge (). Physics packages contain convection schemes, whose purpose is to remove gravitational instabilities through subgrid-scale vertical mixing. Since the idealized Held-Suarez physics does not contain a convection scheme, the dynamical core tends to be more active in removing gravitational instability, compared to a full physics configuration. Note that the implications of this finding are that one can accept a level of grid-imprinting in the modified Held-Suarez configuration, and trust that it will be absent in more real-world configurations.

Through the use of the physics grid, grid imprinting due to topographic flow is reduced (Figures 11 and 12). The native topography lives on the physics grid, and the surface geopotential is mapped to the nodal points at runtime in *ne30pg3*. The mapping method does not introduce new extreme to the nodal points, and the topography tends to be smoother at the element boundaries, relative to *ne30np4*. In regions of gravitational instability, the



flow is damped compared to the *ne30np4* configuration. Gravitational instability results in large magnitude physics tendencies (predominantly grid-scale condensation), whch are damped at element boundaries through the use of the physics grid (Figure ??).

Acknowledgments. NCAR is sponsored by the National Science Foundation (NSF).

References

- Arakawa, A., and W. H. Schubert, 1974: Interaction of a cumulus cloud ensemble with the large-scale environment, Part I. *J. Atmos. Sci.*, **31**, 674–701.
- Bacmeister, J. T., M. F. Wehner, R. B. Neale, A. Gettelman, C. Hannay, P. H. Lauritzen, J. M. Caron, and J. E. Truesdale, 2013: Exploratory high-resolution climate simulations using the community atmosphere model (cam). *J. Climate*, **27** (9), 3073–3099, doi: 10.1175/JCLI-D-13-00387.1.
- Brdar, S., M. Baldauf, A. Dedner, and R. Klfkorn, 2013: Comparison of dynamical cores for nwp models: comparison of cosmo and dune.

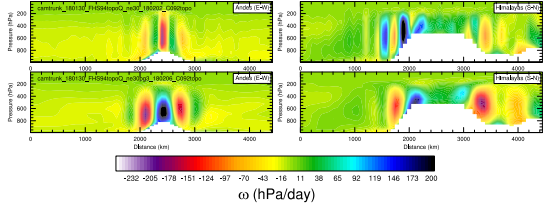


FIG. 12. Great circle distance-pressure transect of *omega* in the Held-Suarez simulations with realistic topography. *omega* field derived from the final 12 months of a 13 month simulation.

Theoretical and Computational Fluid Dynamics, **27** (3-4), 453–472, doi:10.1007/s00162-012-0264-z.

Dennis, J. M., and Coauthors, 2012: CAM-SE: A scalable spectral element dynamical core for the Community Atmosphere Model. *Int. J. High. Perform. C.*, **26** (1), 74–89, doi:10.1177/1094342011428142, URL <http://hpc.sagepub.com/content/26/1/74.abstract>, <http://hpc.sagepub.com/content/26/1/74.full.pdf+html>.

Durran, D., 2010: *Numerical Methods for Fluid Dynamics: With Applications to Geophysics*, Texts in Applied Mathematics, Vol. 32. 2nd ed., Springer, 516 p.

Fournier, A., M. A. Taylor, and J. J. Tribbia, 2004: The spectral element atmosphere model (SEAM): High-resolution parallel computation and localized resolution of regional dynamics. *Mon. Wea. Rev.*, **132** (3), 726–748.

Giraldo, F., and M. Restelli, 2008: A study of spectral element and discontinuous galerkin methods for the Navier-Stokes equations in nonhydrostatic mesoscale atmospheric modeling: Equation sets and test cases. *J. Comput. Phys.*, **227** (8), 3849 – 3877, doi:<http://dx.doi.org/10.1016/j.jcp.2007.12.009>.

Guba, O., M. A. Taylor, P. A. Ullrich, J. R. Overfelt, and M. N. Levy, 2014: The spectral element method (sem) on variable-resolution grids: evaluating grid sensitivity and resolution-aware numerical viscosity. *Geosci. Model Dev.*, **7** (6), 2803–2816, doi:10.5194/gmd-7-2803-2014.

Held, I. M., and M. J. Suarez, 1994: A proposal for the intercomparison of the dynamical cores of atmospheric general circulation models. *Bull. Am. Meteorol. Soc.*, **73**, 1825–1830.

Kim, Y.-J., F. X. Giraldo, M. Flatau, C.-S. Liou, and M. S. Peng, 2008: A sensitivity study of the kelvin wave and the Madden-Julian oscillation in aquaplanet simulations by the Naval Research Laboratory Spectral Element Atmospheric Model. *J. Geo. Res.: Atmospheres*, **113** (D20), doi:10.1029/2008JD009887, d20102.

Lauritzen, P. H., and Coauthors, 2017: Ncar cesm2.0 release of camse: A reformulation of the spectral-element dynamical core in dry-mass vertical coordinates with comprehensive treatment of condensates and energy. *J. Adv. Model. Earth Syst.*, in prep.

Medeiros, B., D. L. Williamson, and J. G. Olson, 2016: Reference aquaplanet climate in the community atmosphere model, version 5. *J. Adv. Model. Earth Syst.*, **8** (1), 406–424, doi:10.1002/2015MS000593.

Nair, R., H.-W. Choi, and H. Tufo, 2009: Computational aspects of a scalable high-order discontinuous galerkin atmospheric dynamical core. *Computers & Fluids*, **38** (2), 309 – 319, doi:<http://dx.doi.org/10.1016/j.compfluid.2008.04.006>.

Nair, R. D., M. N. Levy, and P. H. Lauritzen, 2011: Emerging numerical methods for atmospheric modeling, in: P.H. Lauritzen, R.D. Nair, C. Jablonowski, M. Taylor (Eds.), Numerical techniques for global atmospheric models. *Lecture Notes in Computational Science and Engineering*, Springer, **80**.

Neale, R. B., and B. J. Hoskins, 2000: A standard test for agcms including their physical parametrizations: I: the proposal. *Atmos. Sci. Lett.*, **1** (2), 101–107, doi:10.1006/asle.2000.0022.

Neale, R. B., and Coauthors, 2010: Description of the NCAR Community Atmosphere Model (CAM 5.0). NCAR Technical Note, National Center of Atmospheric Research.

Reed, K. A., J. T. Bacmeister, N. A. Rosenbloom, M. F. Wehner, S. C. Bates, P. H. Lauritzen, J. E. Truesdale, and C. Hannay, 2015: Impact of the dynamical core on the direct simulation of tropical cyclones in a high-resolution global model. *Geophys. Res. Lett.*, **42** (9), 3603–3608, doi:10.1002/2015GL063974.

Rhoades, A. M., X. Huang, P. A. Ullrich, and C. M. Zarzycki, 2016: Characterizing sierra nevada snowpack using variable resolution cesm. *J. Appl. Meteor. Climatol.*, **55**, doi:10.1175/JAMC-D-15-0156.1, URL <http://dx.doi.org/10.1175/JAMC-D-15-0156.1>.

Small, R. J., and Coauthors, 2014: A new synoptic scale resolving global climate simulation using the community earth system model. *Journal of Advances in Modeling Earth Systems*, **6** (4), 1065–1094, doi:10.1002/2014MS000363.

Taylor, M., J. Edwards, and A. St-Cyr, 2008: Petascale atmospheric models for the community climate system model: new developments and evaluation of scalable dynamical cores. *J. Phys.: Conf. Ser.*, **125**, doi:10.1088/1742-6596/125/1/012023.

Taylor, M. A., and A. Fournier, 2010: A compatible and conservative spectral element method on unstructured grids. *J. Comput. Phys.*, **229** (17), 5879 – 5895, doi:10.1016/j.jcp.2010.04.008.

Ullrich, P. A., and M. A. Taylor, 2015: Arbitrary-order conservative and consistent remapping and a theory of linear maps: Part I. *Mon. Wea. Rev.*, **143**, 2419–2440, doi:10.1175/MWR-D-14-00343.1.

Zarzycki, C. M., C. Jablonowski, and M. A. Taylor, 2014a: Using variable-resolution meshes to model tropical cyclones in the community atmosphere model. *Mon. Wea. Rev.*, **142** (3), 1221–1239, doi: 10.1175/MWR-D-13-00179.1.

Zarzycki, C. M., M. N. Levy, C. Jablonowski, J. R. Overfelt, M. A. Taylor, and P. A. Ullrich, 2014b: Aquaplanet experiments using cam's variable-resolution dynamical core. *J. Climate*, **27** (14), 5481–5503, doi:10.1175/JCLI-D-14-00004.1.

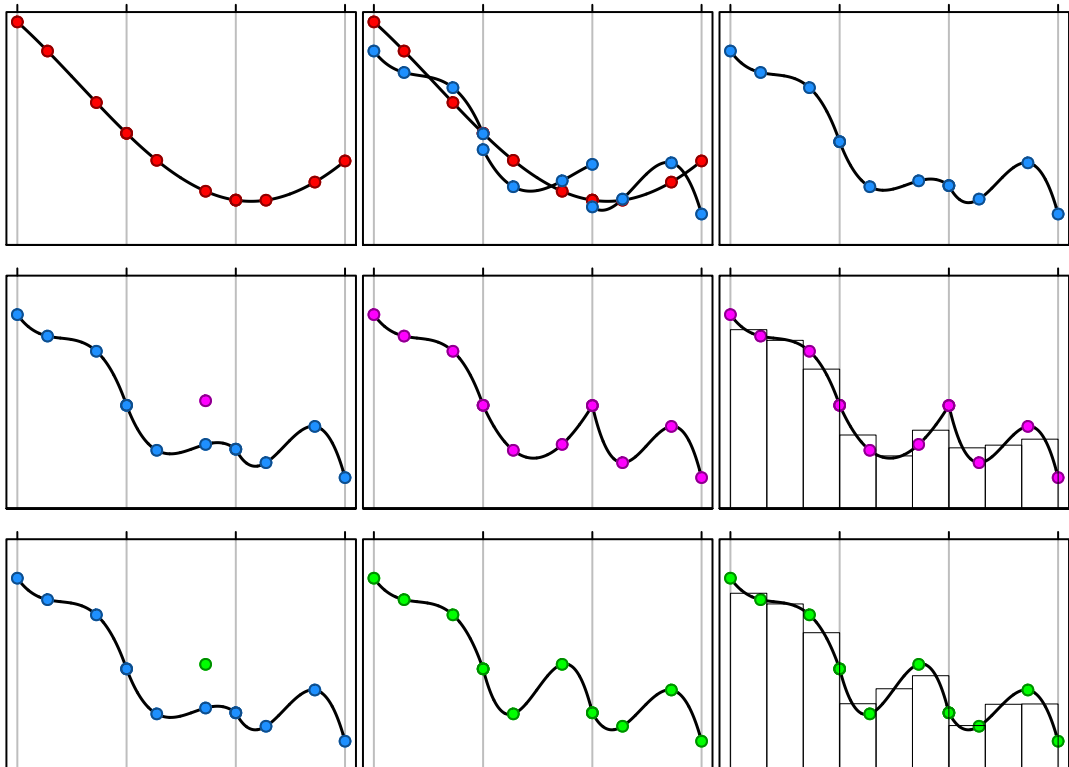


FIG. 4. A 1D schematic illustration on how CAM-SE advances the solution to the equations of motion in time. Consider 3 elements. The red filled circles are the GLL quadrature points in each element ($np = 4$). Note that the quadrature points on the boundary are shared between elements. (a) Assume a degree 3 global Lagrange polynomial initial condition (red curve) which can be represented exactly by the degree 3 Lagrange basis in each element. (b) The solution to the equations of motion are advanced in time (one Runge-Kutta step) independently in each element leading to the quadrature values marked with filled purple circles. The Lagrange basis is shown with red curves connecting the purple circles. There are now two solutions, one from left and one from right, for the quadrature points at the element end points. In CAM-SE the values are averaged so that the solution is C^0 . Note that the averaging changes the Lagrange polynomials throughout except at the internal quadrature points. (c) shows the solution after averaging. (d) Assume there is a grid-scale forcing that increases the quadrature value located at $x = 3$. (e) The solution is now clearly C^0 at the element boundary at $x = 3$. (f) Histogram shows the average values resulting in integrating the basis functions over the control

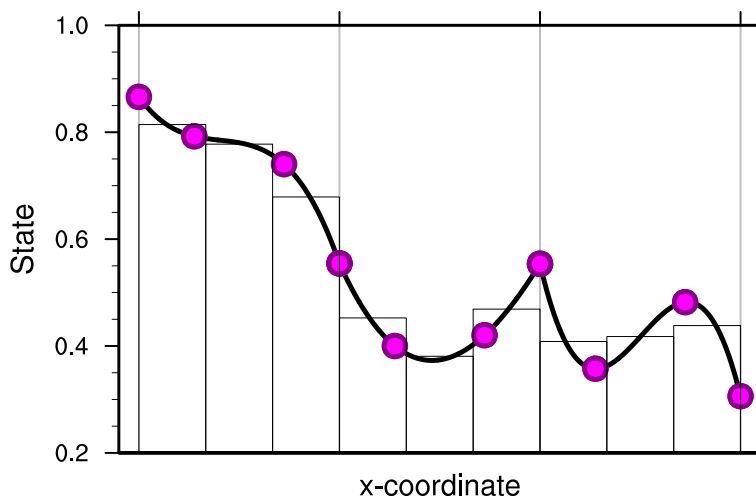


FIG. 5. A graphical illustration of the physics grid in one dimension. Three elements are shown and the filled red circles are the GLL quadrature points in each element. The red curve is the basis function representation of the field and the green filled circles are the quadrature point values. The physics grid divides each element into 3 equal-area control volumes. The histogram shows the average values over the physics grid control volumes resulting from integrating the basis functions over the respective control volumes.